experiment thus invites replication with other outgroups.

The intervention's durable effect on support for a nondiscrimination law also suggests optimism for the public sphere. Over the past century, political campaigns have increasingly relied on mass communication to reach voters (*31*). However, facing difficulty persuading a polarizing public with these strategies (*22*), campaigns increasingly eschew making the case for their positions and instead focus on rousing enthusiasm of voters who already agree with them (*32*). These shifts undermine basic aspirations for democratic discourse. However, these findings suggest that it may be in campaigns' own best interest to place renewed emphasis on a personal exchange of initially opposing views, even regarding controversial issues and across partisan lines.

REFERENCES AND NOTES

1. American Psychological Association, Declaration for the UN World Conference Against Racism, Racial Discrimination, Xenophobia, and Related Intolerance (2001; www.apa.org/pi/oema/programs/racism/apa-delegation-report.pdf).
2. R. D. Enos, *Proc. Natl. Acad. Sci. U.S.A.* **111**, 3699–3704 (2014).
3. T. F. Pettigrew, *Annu. Rev. Sociol.* **24**, 77–103 (1998).
4. E. L. Paluck, D. P. Green, *Annu. Rev. Psychol.* **60**, 339–367 (2009).
5. D. O. Sears, C. L. Funk, *J. Polit.* **61**, 1–28 (1999).
6. M. Tesler, *Am. J. Polit. Sci.* **59**, 806–824 (2015).
7. E. L. Paluck, *J. Pers. Soc. Psychol.* **96**, 574–587 (2009).
8. E. L. Paluck *et al.*, *PLOS ONE* **10**, e0138610 (2015).
9. S. W. Cook, in *Nebraska Symposium on Motivation*, W. J. Arnold, D. Levine, Eds. (Univ. of Nebraska Press, 1969), pp. 179–236.
10. C. V. Laar, S. Levin, S. Sinclair, J. Sidanius, *J. Exp. Soc. Psychol.* **41**, 329–345 (2005).
11. R. E. Petty, C. P. Haugtvedt, S. M. Smith, in *Attitude Strength: Antecedents and Consequences*, R. E. Petty, J. A. Krosnick, Eds. (Erlbaum Associates, Mahwah, NJ, 1995), pp. 93–130.
12. G. Ku, C. S. Wang, A. D. Galinsky, *Res. Organ. Behav.*, 10.1016/j.riob.2015.07.003 (2015).
13. A. D. Galinsky, G. B. Moskowitz, *J. Pers. Soc. Psychol.* **78**, 708–724 (2000).
14. A. R. Flores, *Polit. Groups Identities* **3**, 398–416 (2015).
15. M. Fernandez, A. Blinder, Opponents of Houston rights measure focused on bathrooms, and won, *N.Y. Times* (4 Nov. 2015); available at www.nytimes.com/2015/11/05/us/houston-anti-discrimination-bathroom-ordinance.html (accessed 25 Jan. 2016).
16. H. Gehlbach, M. E. Brinkworth, *Teach. Coll. Rec.* **114**, 226–254 (2012).
17. D. W. Nickerson, T. Rogers, *Psychol. Sci.* **21**, 194–199 (2010).
18. E. J. Finkel, E. B. Slotter, L. B. Luchies, G. M. Walton, J. J. Gross, *Psychol. Sci.* **24**, 1595–1601 (2013).
19. D. W. Nickerson, *Polit. Anal.* **13**, 233–252 (2005).
20. K. Sherrill, *PS Polit. Sci. Polit.* **29**, 469–473 (1996).
21. A. S. Yang, *Public Opin. Q.* **61**, 477–507 (1997).
22. A. S. Gerber, J. G. Gimpel, D. P. Green, D. R. Shaw, *Am. Polit. Sci. Rev.* **105**, 135–150 (2011).
23. J. R. Zaller, *The Nature and Origins of Mass Opinion* (Cambridge Univ. Press, 1992).
24. D. Chong, J. N. Druckman, *Annu. Rev. Polit. Sci.* **10**, 103–126 (2007).
25. S. J. Hill, J. Lo, L. Vavreck, J. Zaller, *Polit. Commun.* **30**, 521–547 (2013).
26. A. R. Todd, A. D. Galinsky, *Soc. Personality Psychol. Compass* **8**, 374–387 (2014).
27. M. J. LaCour, D. P. Green, *Science* **346**, 1366–1369 (2014).
28. M. McNutt, *Science* **348**, 1100 (2015).
29. H. McGee, Personal route to reach public central to Yes campaign, *Irish Times* (14 May 2015); available at www.irishtimes.com/news/politics/personal-route-to-reach-public-central-to-yes-campaign-1.2211282 (accessed 25 Jan. 2016).
30. H. Han, *How Organizations Develop Activists: Civic Associations and Leadership in the 21st Century* (Oxford Univ. Press, 2014).
31. T. Skocpol, *Diminished Democracy: From Membership to Management in American Civic Life* (Univ. of Oklahoma Press, 2003).
32. C. Panagopoulos, *Party Polit.* **22**, 179–190 (2015).

ACKNOWLEDGMENTS

The authors acknowledge funding from the Gill Foundation for this research. D.B. acknowledges the National Science Foundation Graduate Research Fellowship Program for support while conducting this research. Replication data and code are available at http://dx.doi.org/10.7910/DVN/WKR39N. Neither of the authors is affiliated with the Los Angeles LGBT Center or SAVE or received compensation for this research. A preanalysis plan was filed after the data were collected but before they were analyzed with the treatment indicator, and revised preanalysis plans were also filed before the 3-week and 6-week surveys. These are available at the Evidence in Governance and Politics site (www.egap.org), ID 20150707AA. This research was approved by the University of California–Berkeley Committee for the Protection of Human Subjects, Protocol ID 2015-04-7508.

SUPPLEMENTARY MATERIALS

www.sciencemag.org/content/352/6282/220/suppl/DC1
Materials and Methods
Fig. S1
Tables S1 to S25
References (*33*–*49*)

30 November 2015; accepted 17 February 2016
10.1126/science.aad9713

CLIMATE CHANGE

Observational constraints on mixed-phase clouds imply higher climate sensitivity

Ivy Tan,[1]* Trude Storelvmo,[1] Mark D. Zelinka[2]

Global climate model (GCM) estimates of the equilibrium global mean surface temperature response to a doubling of atmospheric CO_2, measured by the equilibrium climate sensitivity (ECS), range from 2.0° to 4.6°C. Clouds are among the leading causes of this uncertainty. Here we show that the ECS can be up to 1.3°C higher in simulations where mixed-phase clouds consisting of ice crystals and supercooled liquid droplets are constrained by global satellite observations. The higher ECS estimates are directly linked to a weakened cloud-phase feedback arising from a decreased cloud glaciation rate in a warmer climate. We point out the need for realistic representations of the supercooled liquid fraction in mixed-phase clouds in GCMs, given the sensitivity of the ECS to the cloud-phase feedback.

Mixed-phase clouds, ubiquitous in Earth's atmosphere (*1*) at temperatures between 0° and −40°C, strongly influence Earth's radiation budget (*2*–*4*). For a fixed amount of cloud water, spherical liquid droplets tend to be smaller in size (*5*) and also to outnumber ice crystals, because ice nuclei (IN) are relatively scarce in Earth's atmosphere in comparison to cloud condensation nuclei (*6*). As a consequence, clouds that consist of a higher fraction of liquid are optically thicker and hence more reflective of sunlight. Here we refer to the fraction of supercooled liquid within a mixed-phase cloud at a particular isotherm as the supercooled liquid fraction (SLF).

It has recently been shown that SLFs are severely underestimated on a global scale in a multitude of global climate models (GCMs) (*7*, *8*). This arises from two main causes. The first cause concerns the challenge of representing the microscopic nature of the various mixed-phase cloud processes (*9*) that cannot be resolved at the typical spatial scales of GCMs. The Wegener-Bergeron-Findeisen (WBF) process for ice crystal growth is one such process that critically affects SLFs (*8*, *10*–*12*). This process refers to the growth of ice crystals at the expense of surrounding supercooled liquid droplets in a mixed-phase cloud as a consequence of the lower saturation vapor pressure over ice relative to liquid. An ambient vapor pressure in between the saturation vapor pressures over liquid and ice is both a necessary and sufficient condition for the WBF process to occur in mixed-phase clouds (*5*). GCMs typically parameterize the WBF process by assuming homogeneous mixtures of supercooled liquid droplets and ice crystals within a model gridbox (*10*, *11*). However, in situ observations suggest that such mixtures rarely exist in nature. Instead, pockets composed purely of either supercooled liquid droplets or ice crystals that are orders of magnitude smaller than the volume of a typical GCM gridbox are suggested to be the norm (*13*, *14*). This implies that the WBF process may be too efficient in GCMs and is thus potentially a culprit for the underestimation of SLFs in GCMs. The multiple modes of ice nucleation (*5*), further complicated by the uncertainty associated with the efficiency

[1]Department of Geology and Geophysics, Yale University, New Haven, CT 06511, USA. [2]Program for Climate Model Diagnosis and Intercomparison, Lawrence Livermore National Laboratory, Livermore, CA 94550, USA.
***Corresponding author. E-mail: ivy.tan@yale.edu**

of the various IN species (*15*), are additional factors contributing to the uncertainties in SLFs.

The second cause concerns the fact that mixed-phase clouds are poorly constrained because of the difficulty of obtaining observations of these clouds (*16*, *17*). Although mixed-phase clouds are ubiquitous in Earth's mid- and high latitudes (*1*), in situ observations of these clouds are naturally limited by sparse spatial and temporal coverage. Technical difficulties in distinguishing liquid and ice particles of varying sizes, as well as artefacts associated with ice crystal shattering on probes (*18*), further complicate this matter. Satellite observations by NASA's Cloud-Aerosol Lidar with Orthogonal Polarization (CALIOP) instrument (*19*) offer an attractive alternative by providing global measurements of cloud thermodynamic phases since 2006.

To address the aforementioned issues, we constrained cloud phase in version 5.1 of the National Center for Atmospheric Research's Community Atmosphere Model (CAM5.1) (*20*) by using 79 months of observations obtained by CALIOP. CAM5.1 is a state-of-the-art GCM, used for climate studies worldwide, and is among the GCMs that severely underestimate SLFs over the entire globe relative to satellite observations (*7*, *8*). To constrain CAM5.1-simulated SLFs to agree with observations, we adopted a quasi–Monte Carlo sampling approach to select 256 combinations of six cloud microphysical parameters (table S1), among which we included the WBF process time scale for the growth of ice crystals and the fraction of atmospheric aerosols active as IN (*12*). The WBF process is rendered less efficient in each case by retarding the time scale at which the process occurs. The default CAM5.1 ice nucleation scheme is replaced with one that has been developed based on in situ surface and aircraft observations to prognostically calculate the ice nucleating-particle concentration using the concentration of large dust aerosols (*21*). Out of the 256 simulations, two parameter combinations (table S1) that yield root mean square errors of SLF < 0.050 across all isotherms were implemented into the fully coupled version of CAM5.1, CESM, version 1.0.6 (*22*), which includes interactive full-depth ocean, sea-ice, and land components. To benchmark these satellite-constrained simulations (hereafter referred to as CALIOP-SLF1 and CALIOP-SLF2), fully coupled simulations using the default model run without any modifications (henceforth referred to as control), as well as two more cases with unrealistically high and low SLFs meant to serve as the upper and lower bounds (henceforth referred to as high-SLF and low-SLF, respectively), were also run until the global net radiation budget at the top of the atmosphere was balanced with both present-day and doubled CO_2 concentrations, totaling 10 simulations altogether (table S2 and fig. S1). The simulated climate states are within realistic bounds (table S2). SLFs henceforth refer to those averaged over the past 50 years of simulation (the "mean state") with present-day CO_2 concentrations (the "initial state").

The mean extratropical (poleward of 30°) SLFs of the five cases are compared against each other in Fig. 1A, along with their ECS estimates in Fig. 1B. The correlation between SLF and ECS is evident upon comparison of the two figures [Pearson correlation coefficient (R) = 0.98, P = 0.0025]. The ECS estimates monotonically increase with increasing initial-state SLF, exhibiting a range extending from 3.9°C in low-SLF to 5.7°C in high-SLF. The ECS values of the other three cases exhibit a wide range of values in between these two unrealistic extremes. The control case has an ECS of 4.0°C, which is significantly lower than the satellite-constrained cases of 5.0° and 5.3°C, for CALIOP-SLF1 and CALIOP-SLF2, respectively. This result suggests that GCMs that underestimate SLFs may also be severely underestimating ECS. The upper bound of the observationally constrained estimates is greater than that of 30 GCMs participating in the Coupled Model Intercomparison Project (CMIP, version 5) (*23*). It should be noted, however, that the ECS estimates of these 30 GCMs were computed using different methods and thus may not be directly comparable with the estimates presented here.

This increase in the ECS estimates is directly linked to a weakened negative cloud-phase feedback that affects shortwave (SW) more strongly than longwave (LW) radiation (*2*). In this feedback, an initial doubling of CO_2 concentrations causes the entire troposphere to deepen. In response, isotherms throughout the troposphere will shift upward in altitude relative to their location in the initial state. This implies that at any fixed altitude, there is a greater likelihood that the SLF of any mixed-phase cloud occupying that altitude will be higher than that of any pre-existing cloud at the same altitude in the initial state. Because mixed-phase clouds with higher SLFs are more reflective of SW radiation than those with lower SLFs, the enhanced reflection of SW radiation back to space counteracts the CO_2-induced warming. The cloud-phase feedback becomes less pronounced for mixed-phase clouds with higher initial-state SLFs (*24*). To illustrate this effect in the extreme, the feedback effectively vanishes for mixed-phase clouds with SLFs of unity, a scenario that is analogous to what occurs in high-SLF (Fig. 2, A and C). Here, the replacement of ice with liquid after CO_2 doubling only occurs between temperatures extending from ~ –30°C down to –40°C, which is approximately the temperature threshold for homogeneous freezing of liquid droplets. Furthermore, its strength is weakened by the fact that less cloud condensate exists at colder temperatures. As the negative cloud-phase feedback weakens, it is less effective at compensating for other processes that reduce cloud optical depth, which may include the drying of cloud layers by convective mixing (*25*) and rapid cloud adjustments to CO_2 (*26*). At the other extreme is low-SLF, which exhibits the strongest cloud-phase feedback (Fig. 2, B and D). Here, the feedback occurs throughout the heterogeneous freezing temperatures (0° to ~ –40°C). Although the cloud-phase feedback operates at all latitudes, it is strongest in the extratropics. At high latitudes, its effect on SW radiation is muted by the polar night.

The change in the gridbox-averaged liquid water path (ΔLWP), which measures the change in vertically integrated cloud liquid water content under global warming, monotonically decreases with increasing initial-state SLF (Fig. 1C). This is consistent with a weakening of the cloud-phase feedback. Although ΔLWP is positive in low-SLF, control, and CALIOP-SLF1 simulations, it eventually becomes negative in CALIOP-SLF2 and high-SLF, when the cloud-phase feedback has weakened to the point that other mechanisms cause the overall negative ΔLWP.

The mean extratropical net cloud optical depth feedback (λ_τ) quantifies the extent to which changes in the cloud optical depth amplify ($\lambda_\tau > 0$) or damp ($\lambda_\tau < 0$) the initial warming response to CO_2 doubling. The cloud-phase feedback is a primary but not the sole contributor to the cloud optical depth feedback by virtue of the vastly different optical depths of liquid and ice clouds

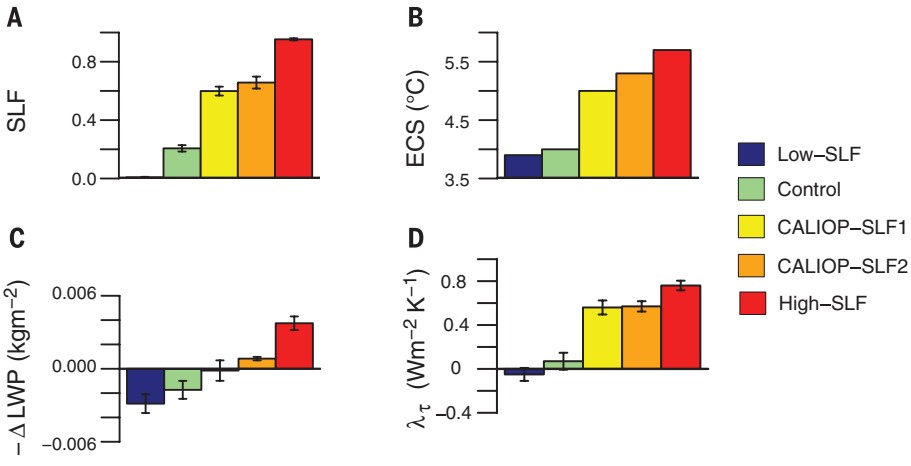

Fig. 1. The link between cloud thermodynamic phase partitioning and ECS. Error bars represent the 1σ confidence interval. (**A**) The initial-state extratropical SLFs at the –10°C isotherm. (**B**) ECS estimates in response to CO_2 doubling. (**C**) Changes in global mean gridbox-average LWP. (**D**) Mean extratropical net cloud optical depth feedback, λ_τ.

(5). The monotonic increase in λ_τ is also consistent with a monotonic weakening of the cloud-phase feedback with increasing SLF (Fig. 1D). λ_τ is calculated based on the cloud radiative kernel method (27), using cloud fractions derived from the International Satellite Cloud Climatology Project satellite simulator (28, 29) implemented in CAM5.1. This method allows the total cloud feedback to be decomposed into individual contributions from the changes in cloud optical depth (λ_τ) and cloud-top pressure (i.e. height; λ_{CTP}) and fraction (λ_{Amt}). Although the sum $\lambda_{CTP} + \lambda_{Amt}$ remains within 7% of that of the control across all cases, λ_τ monotonically increases with increasing SLF over a wide range primarily because of differences in reflected SW radiation (Fig. 3A). Regressions of cloud and noncloud feedbacks on ECS also strongly suggest that the cloud-phase feedback is driving the spread in ECS through its relation to λ_τ (fig. S2).

Global distributions of λ_τ elucidate the strength and locations over which the negative cloud-phase feedback occurs. The negative cloud-phase feedback is strongest in low-SLF, and the high latitudes of both hemispheres show corresponding strongly negative λ_τ values (Fig. 3B). The weaker negative cloud-phase feedback in the control case exhibits less negative λ_τ values over the high latitudes (Fig. 3C). Eventually, the negative cloud-phase feedback is weakened to the extent that high-latitude λ_τ values become increasingly positive through the manifestation of other warming mechanisms in this order:

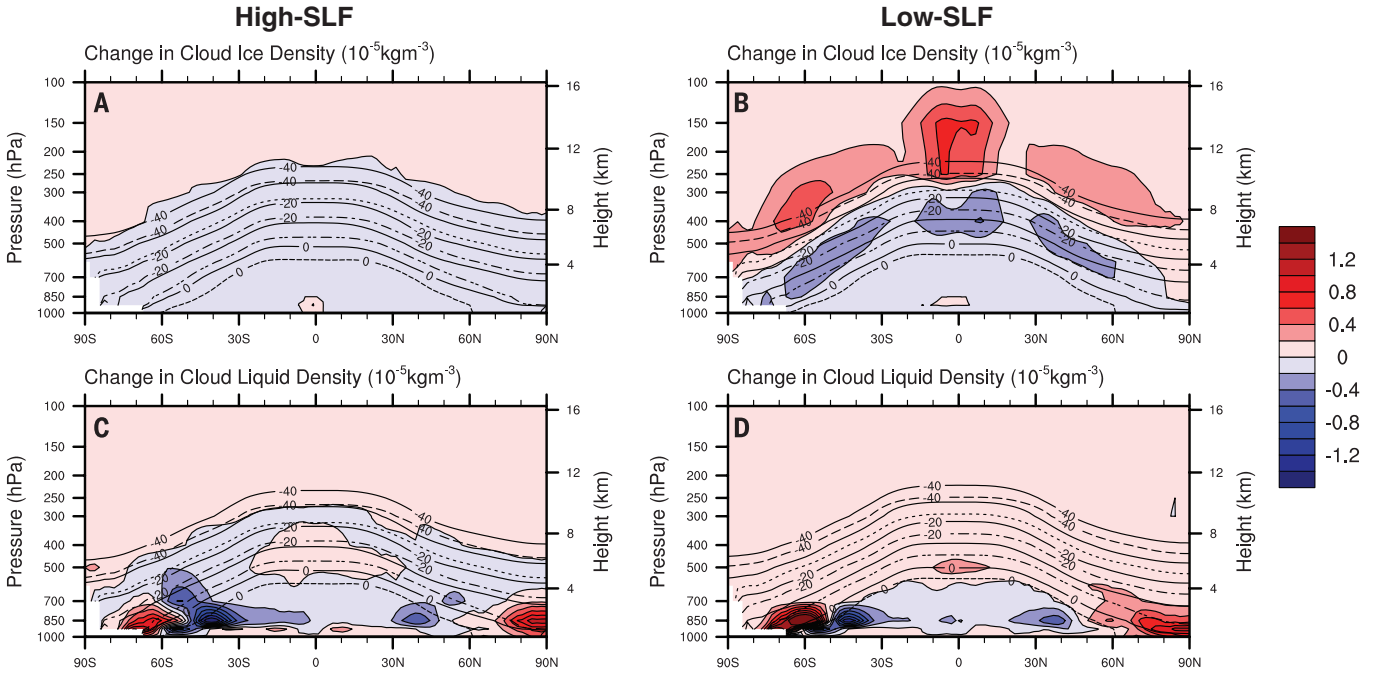

Fig. 2. Weakening of the cloud-phase feedback. Pressure-latitude cross-sections of zonal mean-state changes in gridbox-averaged (**A** and **B**) cloud ice and (**C** and **D**) cloud liquid densities in [(A) and (C)] high-SLF and [(B) and (D)] low-SLF in response to CO_2 doubling, exemplifying weakening of the cloud-phase feedback. Isotherms in the present-day CO_2 simulations are displayed as dashed lines; isotherms in the doubled CO_2 simulations are displayed as solid lines. The quantity of ice throughout the mixed-phase clouds in low-SLF decreases upon CO_2 doubling, while the quantity of liquid increases. The feedback still occurs in high-SLF, but it is substantially weakened, occurring only at the coldest isotherm.

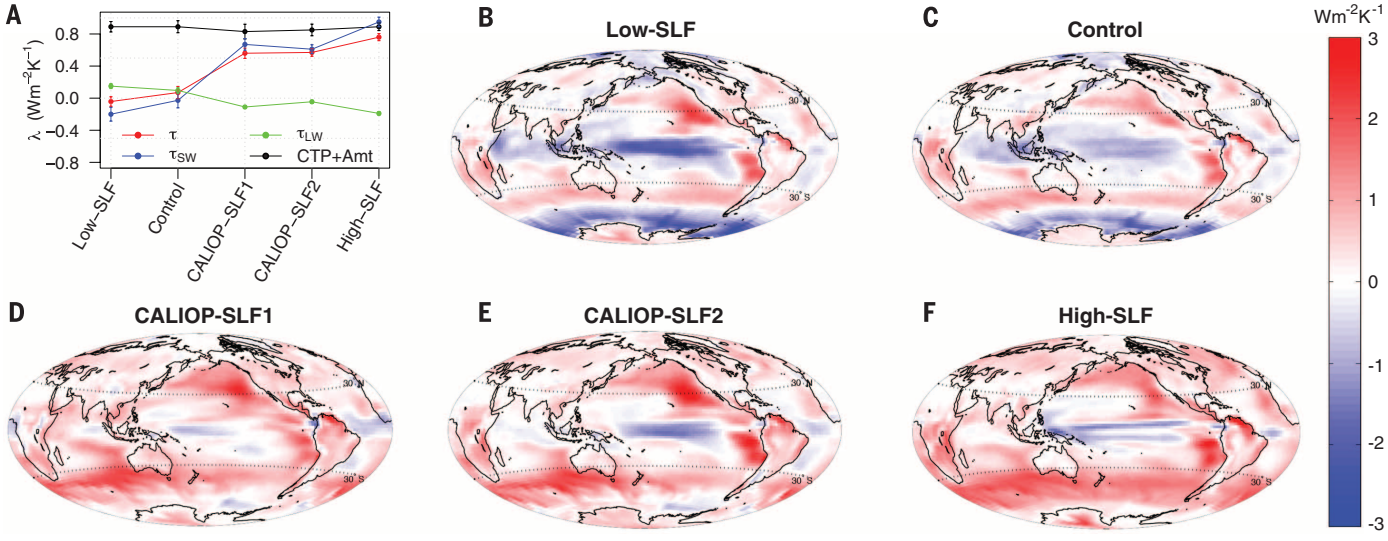

Fig. 3. Increase in the net cloud optical depth feedback parameter λ_τ with increasing initial mean-state SLF. Error bars represent the 1σ confidence interval. (**A**) Mean net extratropical λ_τ, decomposed into its SW and LW components, alongside the sum of the mean net extratropical λ_{CTP} and λ_{Amt}. (**B** to **F**) Global distributions of λ_τ.

CALIOP-SLF1 (Fig. 3D), CALIOP-SLF2 (Fig. 3E), and high-SLF (Fig. 3F). It is worth noting that the cloud-phase feedback is particularly sensitive to higher initial-state SLFs over the pristine Southern Ocean in the observationally constrained cases. Underestimates of SLFs relative to observations in this region (*30*) lead to an artificially stronger cloud-phase feedback that can ultimately lead to an underestimate of ECS. The negative λ_τ values over the tropical Pacific are attributed to the thickening of high clouds (*27*).

Global satellite observations of cloud thermodynamic phases have enabled us to show that unrealistically low SLFs common to a multitude of GCMs lead to a cloud-phase feedback that is too negative. This has important ramifications for ECS estimates. Should the low-SLF bias be eliminated in GCMs, the most likely range of ECS should shift to higher values. It should be noted that there are variations in the way in which microphysical processes are parameterized in GCMs. Thus, the method by which SLFs can be constrained in GCMs is not unique, and a repeat of this study in other GCMs may thus lead to other climate feedback responses that are not captured by the GCM used in this study. However, regardless of how SLFs are constrained, the SLF will affect the magnitude of the cloud-phase feedback and therefore GCMs' estimates of ECS. Looking forward, continued improvements of the accuracy of various observational methods, better understanding of mixed-phase cloud processes, and their improved representation in GCMs are all factors that are critical to improving the accuracy of ECS estimates.

REFERENCES AND NOTES

1. M. D. Shupe *et al.*, *Bull. Am. Meteorol. Soc.* **89**, 1549–1562 (2008).
2. J. F. B. Mitchell, C. A. Senior, W. J. Ingram, *Nature* **341**, 132–134 (1989).
3. Z. Sun, K. P. Shine, *Q. J. R. Meteorol. Soc.* **120**, 111–137 (1994).
4. Z.-S. Li, H. Le Treut, *Clim. Dyn.* **7**, 133–139 (1992).
5. H. R. Pruppacher, J. D. Klett, *Microphysics of Clouds and Precipitation 1980* (Reidel, Dordrecht, Netherlands, 1978).
6. B. J. Murray, D. O'Sullivan, J. D. Atkinson, M. E. Webb, *Chem. Soc. Rev.* **41**, 6519–6554 (2012).
7. M. Komurcu *et al.*, *J. Geophys. Res.* **119**, 3372–3400 (2014).
8. G. Cesana, D. E. Waliser, X. Jiang, J. L. Li, *J. Geophys. Res.* **120**, 7871–7892 (2015).
9. U. Lohmann, C. Hoose, *Atmos. Chem. Phys.* **9**, 8917–8934 (2009).
10. T. Storelvmo *et al.*, *Environ. Res. Lett.* **3**, 045001 (2008).
11. J. Fan *et al.*, *J. Geophys. Res.* **116**, D00T07 (2011).
12. I. Tan, T. Storelvmo, *J. Atmos. Sci.* **73**, 709–728 (2016).
13. A. Korolev, G. Isaac, S. Cober, J. W. Strapp, J. Hallett, *Q. J. R. Meteorol. Soc.* **129**, 39–65 (2003).
14. P. Chylek, C. Borel, *Geophys. Res. Lett.* **31**, L14104 (2004).
15. J. D. Atkinson *et al.*, *Nature* **498**, 355–358 (2013).
16. A. J. Illingworth *et al.*, *Bull. Am. Meteorol. Soc.* **88**, 883–898 (2007).
17. H. Morrison *et al.*, *Nat. Geosci.* **5**, 11–17 (2012).
18. A. Korolev, E. Emery, J. W. Strapp, S. G. Cober, G. A. Isaac, *J. Atmos. Ocean. Technol.* **30**, 2527–2553 (2013).
19. D. M. Winker *et al.*, *J. Atmos. Ocean. Technol.* **26**, 2310–2323 (2009).
20. R. B. Neale *et al.*, Description of the NCAR Community Atmosphere Model (CAM5.0). *NCAR Tech. Note NCAR/TN-486+STR* (2010).
21. P. J. DeMott *et al.*, *Atmos. Chem. Phys.* **15**, 393–409 (2015).
22. J. W. Hurrell *et al.*, *Bull. Am. Meteorol. Soc.* **94**, 1339–1360 (2013).
23. T. Mauritsen, B. Stevens, *Nat. Geosci.* **8**, 346–351 (2015).
24. Y. Tsushima *et al.*, *Clim. Dyn.* **27**, 113–126 (2006).
25. S. C. Sherwood, S. Bony, J.-L. Dufresne, *Nature* **505**, 37–42 (2014).
26. T. Andrews, J. M. Gregory, P. Forster, M. J. Webb, *Surv. Geophys.* **33**, 619–635 (2012).
27. M. D. Zelinka, S. A. Klein, D. L. Hartmann, *J. Clim.* **25**, 3736–3754 (2012).
28. S. A. Klein, C. Jakob, *Mon. Weather Rev.* **127**, 2514–2531 (1999).
29. M. Webb, C. Senior, S. Bony, J.-J. Morcette, *Clim. Dyn.* **17**, 905–922 (2001).
30. D. T. McCoy, D. L. Hartmann, M. D. Zelinka, P. Ceppi, D. P. Grosvenor, *J. Geophys. Res.* **120**, 9539–9554 (2015).

ACKNOWLEDGMENTS

This work was supported by NASA Headquarters under the NASA Earth and Space Science Fellowship Program, grant NNX14AL07H. We also acknowledge high-performance computing support from Yellowstone provided by National Center for Atmospheric Research's Computational and Information Systems Laboratory, sponsored by NSF under grant 1352417. The effort of M.D.Z. was supported by the Regional and Global Climate Modeling Program of the Office of Science at the U.S. Department of Energy (DOE) under grant DE-SC0012580 and was performed under the auspices of DOE by Lawrence Livermore National Laboratory under contract DE-AC52-07NA27344. CALIOP data are available online at https://eosweb.larc.nasa.gov/order-data. National Centers for Environmental Prediction–DOE Reanalysis 2 data are also available online at www.esrl.noaa.gov/psd/data/gridded/data.ncep.reanalysis2.pressure.html.

SUPPLEMENTARY MATERIALS

www.sciencemag.org/content/352/6282/224/suppl/DC1
Materials and Methods
Figs. S1 and S2
Tables S1 and S2
References (*31*–*37*)

25 September 2015; accepted 3 March 2016
10.1126/science.aad5300

CANCER BIOLOGY

MYC regulates the antitumor immune response through CD47 and PD-L1

Stephanie C. Casey,[1] Ling Tong,[1] Yulin Li,[1] Rachel Do,[1] Susanne Walz,[2] Kelly N. Fitzgerald,[1] Arvin M. Gouw,[1] Virginie Baylot,[1] Ines Gütgemann,[1,3] Martin Eilers,[2,4] Dean W. Felsher[1]*

The *MYC* oncogene codes for a transcription factor that is overexpressed in many human cancers. Here we show that *MYC* regulates the expression of two immune checkpoint proteins on the tumor cell surface: the innate immune regulator CD47 (cluster of differentiation 47) and the adaptive immune checkpoint PD-L1 (programmed death–ligand 1). Suppression of MYC in mouse tumors and human tumor cells caused a reduction in the levels of CD47 and PD-L1 messenger RNA and protein. MYC was found to bind directly to the promoters of the *Cd47* and *Pd-l1* genes. MYC inactivation in mouse tumors down-regulated CD47 and PD-L1 expression and enhanced the antitumor immune response. In contrast, when MYC was inactivated in tumors with enforced expression of CD47 or PD-L1, the immune response was suppressed, and tumors continued to grow. Thus, MYC appears to initiate and maintain tumorigenesis, in part, through the modulation of immune regulatory molecules.

The transcription factor MYC regulates the expression of a multitude of gene products involved in cell proliferation, growth, self-renewal, differentiation, and apoptosis (*1*–*4*). The *MYC* gene is genetically activated and overexpressed in many human cancers (*1*–*4*), and this overexpression has been causally linked to tumorigenesis (*5*, *6*). Studies involving inducible transgenic mouse models have shown that growth of *Myc*-induced tumors is dependent on continuous expression of MYC (*1*–*4*, *7*–*10*). For example, in the tetracycline-off mouse model (where *Myc* expression can be turned off by the addition of tetracycline or doxycycline), tumors grow only when *Myc* is "on." When *Myc* is turned "off," tumors regress.

In mouse models, MYC inactivation results in tumor regression through the induction of proliferative arrest and apoptosis (*1*–*3*, *7*, *8*, *10*–*12*). We have demonstrated that complete tumor clearance that occurs after the inactivation of oncogenes, including *Myc*, requires the recruitment of $CD4^+$ T cells and the secretion of thrombospondin-1 (*13*, *14*). Hence, a host-dependent immune response is required for sustained tumor regression. However, the mechanism by which oncogene inactivation elicits this immune response is unknown.

The host immune system generally serves as a barrier against tumor formation (*15*). Activation of the immune response can contribute to tumor regression (*13*, *16*, *17*) through both adaptive and innate immune effectors (*18*–*20*). Programmed death–ligand 1 (or PD-L1, also known as CD274 and B7-H1) sends a critical "don't find me" signal to the adaptive immune system (*21*–*23*), whereas CD47 (cluster of differentiation 47) sends a critical "don't eat me" signal to the innate immune system and acts as a regulator of the adaptive immune response (*24*, *25*) (fig. S1A). These and similar molecules are often overexpressed on human tumors (*22*, *25*). Therapeutic suppression of PD-L1

[1]Division of Oncology, Departments of Medicine and Pathology, Stanford University School of Medicine, Stanford, CA 94305, USA. [2]Comprehensive Cancer Center Mainfranken, Core Unit Bioinformatics, Biocenter, University of Würzburg, Am Hubland, 97074 Würzburg, Germany. [3]Institute of Pathology, University Hospital Bonn, 53127 Bonn, Germany. [4]Theodor Boveri Institute, Biocenter, University of Würzburg, Am Hubland, 97074 Würzburg, Germany.
***Corresponding author. E-mail: dfelsher@stanford.edu**

Observational constraints on mixed-phase clouds imply higher climate sensitivity

Ivy Tan *et al.*

Science **352**, 224 (2016);
DOI: 10.1126/science.aad5300